SAND2022-4642C

JSAE 20159137
SAE 2015-YY-YYYY

A High-Fidelity Study of High-Pressure Diesel Injection

Marco Arienti
Sandia National Laboratories

Mark Sussman
Florida State University

ABSTRACT

A study of n-dodecane atomization, in response to the prescribed motion of the needle tip, is presented for a high-pressure, non-cavitating Diesel injector ("Spray A", in the Engine Combustion Network denomination). In the simulations discussed here, the internal and external multiphase flows are seamlessly calculated across the injection orifice using an interface-capturing approach (for the liquid fuel surface) together with an embedded boundary formulation (for the injector's walls). This enables to directly relate the liquid jet spray characteristics (under the assumption of sub-critical flow and with a grid resolution of 3 μm, or 1/30 of the orifice diameter) to the internal geometry of this Bosch injector. Another novel element in this work is the capability of modeling the compressibility of the liquid and the gas phase while maintaining a sharp interface between the two. A realistic equation of state calibrated on n-dodecane is implemented. We study the difference in fuel jet characteristics for the cases of adiabatic and isothermal wall conditions in relation to the temperature variation of n-dodecane and its effects on density and viscosity.

INTRODUCTION

While the atomization of liquid fuels is often crucial in determining the fuel-air mixture formation, which subsequently controls performance and emissions, model inadequacies are presently a major barrier. Progress could be achieved by accurately characterizing the flow immediately outside of the injector's orifice, therefore setting the correct boundary conditions for computer simulations in the combustion chamber. However, one of the key model components, the rate of injection (ROI) of the fuel, is affected by various factors that negatively impact measurements (refer, for instance, to Pickett et al. 2014): the measured ROI has fluctuations that do not present any corresponding identifiable feature in the measured rate of momentum (ROM), even when averaged over a large number of injection samples. Moreover, the expansion of the jet outside the orifice, coupled to the thermal conditions at the wall, can lead to non-trivial variations of density. Finally, small deviations from the nominal shape of the orifice can modify the flow in the sac. Efforts by the Engine Combustion Network (ECN) to characterize a specific set of injectors at given operational conditions have brought together modelers and experimentalists in the attempt to solve this and similar issues.

The results presented here are focused on the role of the aforementioned non-idealities in modeling the ROI at high injection pressure for a well-defined injection device. We propose the time-resolved simulation of the gas-liquid interface inside and outside of the injector as a model-free research tool (albeit very expensive): at least in principle, the main parameter the modeler has control of in this case is only the grid resolution. An example of this approach is the massive simulation of a jet from a single-orifice injector by Shinjo and Umemura (2011). That study only concerned flow external to the injector, and injection velocities of 100 m/s or less, whereas we will consider here the complete geometry of the injector tip and velocities that are five or six times larger. The same larger velocities are considered in a more recent study by Bode et al. (2014), but still in the incompressible limit. The latter reference includes part of the injector geometry in a parametric study of the orifice taper ratio, but with an all-open needle configuration and only for 3 microseconds. For the complete injection period, a comparison of the mass flow rates resulting from the needle's movement with or without needle wobble is presented by Xue et al. (2013), but their simulations are carried out only inside the injector (albeit with a respectable 7.5 μm of minimum grid spacing) and in the context of the Reynolds-Averaged Navier-Stokes (RANS) formulation. In that study, the liquid phase was treated as incompressible but the gas phase was compressible. Additional references can be found in the three aforementioned papers.

We consider the effects of injector's asymmetries, as measured in the lab for the same single-hole injector Robert Bosch LLC, specimen 210675, described in the ECN data archive. We also consider the time-dependent needle operation that leads to the orifice opening. The simulation will cover the early transient of the needle unseating corresponding to the

first 370 μm from needle activation, including 30 μm following the emergence of the liquid from the orifice. Two calculations will be discussed: one with adiabatic boundary conditions at the injector's wall and one with a fixed wall temperature.

NUMERICAL METHOD

This paper synthesizes recent work on compressible, multiphase flow in a model for high-pressure fuel injection that includes the time-varying geometry of the injector and a realistic equation of state for n-dodecane. All the interfaces are captured by the coupled level-set and moment-of-fluid method (CLSMOF) (Jamison et al., 2013). The two-phase compressible Navier-Stokes equations are solved with a new mass-, momentum-, and energy-conserving advection algorithm (Jemison et al., 2014). The injector wall boundaries are represented by the embedded boundary method described by Arienti and Sussman (2014).

In the CLSMOF algorithm, the piecewise-linear interface reconstruction uses information from the level set function, volume of fluid function and reference centroid to produce a slope and an intercept for the local reconstruction of the gas-liquid interface. Maintained at each time step as the signed distance to the reconstructed interface, the level set function is coupled to the volume-of-fluid function and reference centroid. In a comparison with the CLSVOF method previously used by the authors, the accuracy and mass conservation properties of CLSMOF are excellent (Jamison et al., 2013).

The semi-implicit pressure update scheme by Jemison et al. (2014) asymptotically preserves the standard incompressible pressure projection in the limit of infinite sound speed. This attribute makes the new method applicable to compressible flows, including liquids with stiff equations of state, using time steps that can be larger compared to typical explicit methods.

The embedded boundary method uses one more signed distance function, the "solid" level set: its magnitude is the minimal distance between the regular cell center and the surface of the body, and, by convention, the sign is positive outside the body and negative inside it. When applied to the motion of solid interfaces, the embedded boundary sweeps the computational Cartesian cells in a robust manner: thus, contact and separation of boundaries, such as during the unseating of the needle, occur in a very straightforward manner.

Another component of our simulation capability is the use of block-structured, adaptive mesh refinement (AMR). At each new re-gridding operation, Cartesian boxes (with a minimum size of, say, 32^3 cells) are combined to cover all the tagged cells within the assigned coverage efficiency. This set of blocks with the same grid spacing forms level one. The refinement ratio between two consecutive levels is two. The new level can in turn be tagged for refinement, and the process is repeated until the input grid resolution is achieved. Data on the fine level are either copied from a previous time step or, when the grid structure has changed locally, conservatively interpolated from the underlying coarse level. The liquid-gas interface is always embedded in the finest grid level to avoid gross interpolation errors. An extensive discussion can be found in Kadiouglu and Sussman (2008). The definitions and operators necessary to carry out the AMR tasks are provided by the BOXLIB library (CCSE 2012), which is developed and maintained by the Center for Computational Sciences and Engineering group at Lawrence Berkeley National Laboratories.

The computational model outlined above is described in greater detail in the references mentioned here. In the following, we describe more closely only the new elements introduced in the present simulations. The liquid and gas phase properties are evaluated at run-time as a function of pressure, phase density and phase internal energy.

INJECTOR MODEL

INJECTOR PROPERTIES

The walls of the Diesel injector are the only elements that need to be discretized. The wall tessellation is read at the beginning of the simulation as a conventional list of node coordinates and of links. As the SN 210675 Bosch injector used in this test is affected by slight manufacturing defects (the reader is referred to the ECN web site for full documentation), an off-center position with respect to the sac is purposely introduced in the model: the orifice center is displaced by 53 μm at θ = +9° in the convention of Figure 1. This offset means that the inlet-turning angle is lower on one side of the orifice compared to the opposite side. To facilitate the visualization of the effects on the flow, the Cartesian axes of the simulation are rotated by +9°: in other words, the z = 0 cross-sections that will be presented in this work are taken along the direction of the maximum orifice center displacement from the nominal geometry.

The injector is divided in two parts, the needle tip and the cap, as displayed in Figure 2. The unseating of the needle is modeled by its translation with respect to the injector cap according to a specified trajectory. In frame (a) the needle's base is almost completely inside the computational domain (marked by a dashed line), whereas in its fully open position in frame (c) the base of the needle has moved outside. Frame (b) shows an intermediate position and the effect of the deviation from a perfectly axial trajectory: the annular fuel passage is obviously asymmetric at this time.

The trajectory of the needle, discussed in Kastengren et al. (2012), is shown in Figure 3 for the *X*- *Y*- and *Z*-components (continuous, dashed and dotted line, respectively). Time zero corresponds to the instant when the injection command is given: the same reference time is used in our simulations. The overall recorded time that is available from the ECN archive is 5000 μs, but the needle does not actually move for the first 160 μs. Substantial lateral displacements in addition to the nominal axial motion can be observed in Figure 3. The peak needle lift is reached after approximately 900 μm, then reverses direction and closes at approximately 1800 μs. The corresponding needle velocity is of the order of one meter per second or less. The simulation will cover the early transient of the needle unseating corresponding to the first 370 μm from needle activation.

PHASE PROPERTIES

The gas phase is calculated as a perfect gas with the properties of air. The surface tension coefficient for n-dodecane in air is kept constant at 0.024 N/m and the static contact angle on the injector's wall is 90°. The liquid phase is calculated via a number of correlations derived at high pressure by a number of authors. When multiple sources were available, the reference that covered the broadest range of temperature and pressure was chosen for this work. In one occasion, an existing correlation was modified to better match available data, as specified below.

Equation of state of n-dodecane

The liquid phase pressure, $P(\rho,T)$, is calculated using the Tait formulation with the coefficients proposed by Caudwell et al., (2004) for pressures up to 200 MPa in the temperature range 298-473 K:

$$\rho(\mathrm{kg\cdot m^3}) = \frac{\rho_0(\mathrm{kg\cdot m^3})}{\left(1 - A\ln\left[\left(B + (P/\mathrm{MPa})\right)/\left(B + (P_0/\mathrm{MPa})\right)\right]\right)}$$

with A = 0.08998. B depends only on temperature,

$$(B/\mathrm{MPa}) = \sum_{i=0}^{2} b_i\,(T/\mathrm{K})^i,$$

with b_0 = 345.1, b_1 = -1.1458 K^{-1}, b_2 = 0.9837×10^{-3} K^{-2}. The reference density at P_0 = 0.1 MPa is

$$\rho_0(\mathrm{kg\cdot m^3}) = 929.1654 - 0.5174730\,(T/\mathrm{K}) - 3.338672\cdot 10^{-4}(T/\mathrm{K})^2.$$

The internal energy $e(\rho,T)$ is obtained directly from

$$e = \sum_{i=0}^{4} g_i\,(T/\mathrm{K})^i,$$

Dependence from pressure, evaluated from the above expression for density, is introduced in g_1 and g_2:

$$g_0 = 19.94245;$$

$$g_1 = 2.273845 + 7.701613\cdot 10^{-6}\,(P/\mathrm{MPa})\,((P - P_0)/\mathrm{MPa});$$

$$g_2 = -2.279889\cdot 10^{-3} - 3.654273\cdot 10^{-4}((P - P_0)/\mathrm{MPa});$$

$$g_3 = 6.106366\cdot 10^{-6};$$

$$g_4 = -3.266302\cdot 10^{-9}.$$

The inverse problem of finding temperature from known internal energy and density, $T(e, \rho)$, is solved via an iterative method.

Speed of sound

The speed of sound in the liquid phase is calculated from a correlation using the Tait expression

$$\frac{c - c_0}{c} = D\ln\left[\frac{E + P}{E + P_0}\right]$$

The equation uses the reference atmospheric speed of sound

$$c_0 = 4094 - 183.21\cdot(T/\mathrm{K})^{0.5} + 0.07974\cdot(T/\mathrm{K})^{1.5} - 2.348\cdot 10^{-6}\cdot(T/\mathrm{K})^3.$$

The coefficients in the Tait equation are a function of temperature, pressure and carbon number of the fuel (Padilla-Victoria et al., 2013). For pure n-dodecane,

$$D = 0.1652 + 2.510^{-3}\cdot(T/\mathrm{K}) - 5.85\cdot 10^{-4}\,(T/\mathrm{K})\cdot(P/\mathrm{MPa});$$

$$E = -56.91 + 7.3674\cdot 10^{-5}\cdot(T/\mathrm{K})^2 + 0.02260\cdot(T/\mathrm{K}) + 463.5\cdot\exp(-0.001687\cdot(T/\mathrm{K})).$$

The correlation for D was modified by the authors with respect to one proposed by Padilla-Victoria et al., (2013) to obtain a better match with the sound speed values reported by Khasanshin et al. (2003) in the temperature range 293-433 K and for pressures between 0.1 to 140 MPa.

Dynamic viscosity

The dynamic viscosity, $\mu(\rho,T)$, is calculated from the correlation derived for the same range as for viscosity by Caudwell et al. (2004):

$$\mu/(\mathrm{Pa\cdot s}) = \mu^*\cdot\left[4.778\cdot 10^{-9}\{V/(\mathrm{m^3\cdot mol^{-1}})\}^{-2/3}\{M/(\mathrm{kg\cdot mol^{-1}})\}^{1/2}\{T/K\}^{1/2}\right],$$

where V is the molar volume, M is the molar mass, and μ^* is a dimensionless viscosity given by

$$\frac{1}{\mu^*} = \sum_{i=0}^{3} d_i(V/V_0)^i$$

For n-dodecane, the coefficients d_i are: d_0 = 0.321621; d_1 = -0.4803715; d_2 = 0.222206; d_3 = -2.9964626×10^{-2}. V_0 is a temperature-dependent molar core volume given by

$$V_0/(10^{-6}\ \mathrm{m^3\cdot mol^{-1}}) = \sum_{i=0}^{3} e_i(T/\mathrm{K})^i$$

The coefficients e_i are: e_0 = 191.54; e_1 = -0.441338; e_2 = 8.98744×10^{-4}; e_3 = -6.7792×10^{-7}.

SIMULATION SETUP

Calculations were carried out on the Redsky Sandia cluster using (on average) 128 SUN X6275 blades (2.93 GHz dual socket/quad core configuration with 12 GB RAM per compute node) and four of the eight available nodes for a total of 512 cores. The base computational domain is a regular Cartesian 64×64×576 box with the longest side oriented along the injector's axis measuring 1.53 cm (170 times the exit orifice diameter). This size is substantially longer than in similar high-fidelity simulations because we

intend to follow the jet penetration for a longer time period. Three levels of refinement are added to the coarse level obtain the minimum grid spacing of 3.32 μm, corresponding to 27 computational cells across the orifice diameter. At this grid resolution, a stable time step for the flow of interest (occasionally supersonic in the gas phase and subsonic in the liquid phase) is of the order of a nanosecond. Note that, because of dynamic mesh refinement, the total count of cells increases during the simulation. As the fuel makes its way through the orifice and then outside the injector, this number steadily climbs from approximately 7×10^7 to 12×10^7. Still, such a cell count corresponds to a rather coarse representation of the spray compared to the 0.35 μm grid spacing and the 6×10^9 computational cells in the external flow simulation by Shinjo and Umemura (2011).

The typical edge length of the injector's tessellation is of the order of one or two micrometers at the wall edges. The auxiliary grid for the solid level set (described Arienti and Sussman, 2014) has constant spacing of 9 μm. The wall boundary velocities that are necessary to populate the ghost region of the solid are calculated directly by differentiation of the displacement values read from the trajectory file.

The fixed injection pressure of 150 MPa is applied directly as constant boundary value at the boundary face, see Figure 2. While this is a convenient simplification – fluctuations of up to 8 MPa have been reported in Pickett et al. (2013) – it is acceptable for the simulation interval considered here (future studies will include injection pressure variability as well). A fixed exit pressure of 2 MPa is applied to the other five sides of the computational domain box. The initial temperature of the liquid is uniformly 343 K in both the reservoir and the cap. The initial temperature of the gas is 303 K. This is not the reference 900 K temperature prescribed for Spray A, but corresponds to the non-evaporating condition used for radiographic measurements of fuel mass at Argonne (Pickett et al., 2014). In the isothermal wall simulation the wall temperature is T_w = 393 K.

The simulation begins with a partially liquid-filled sac. The volume left to the gas is 0.065 mm^3, or approximately one third of the sac volume. The volume of the cylindrical orifice, of nominal diameter 90 μm, is much smaller, 0.006 mm^3. A partially filled sac setup is motivated by the observation (via long-distance microscopy and high-contrast display) that a gas or vapor jet is ejected from the orifice before the liquid (Pickett et al., 2013). For the same injection configuration that is studied here, the ejection was reported to take place approximately 7 μs before the emergence of the liquid fuel, suggesting that a certain amount of gas or vapor was already in the sac prior to injection. Based on nominal values at 0.1 MPa and 293.15 K (ρ = 748 kg/m^3, μ = 1.344 mPa-s, Caudwell et al., 2004), and for a pressure drop of 148 MPa, the Reynolds number of the flow traversing the orifice is of the order of 3×10^5.

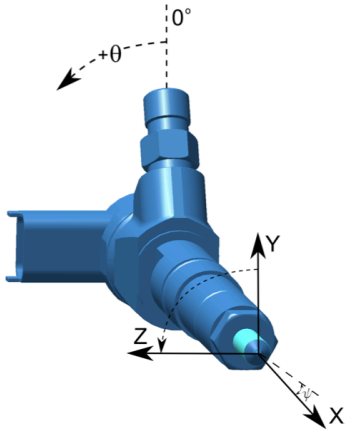

Figure 1. Spray A and reference coordinates.

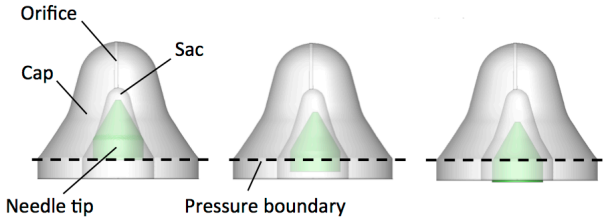

Figure 2. Sequence illustrating the relative motion of the needle tip with respect to the cap. The dashed line is the trace of the boundary plane of the computational domain.

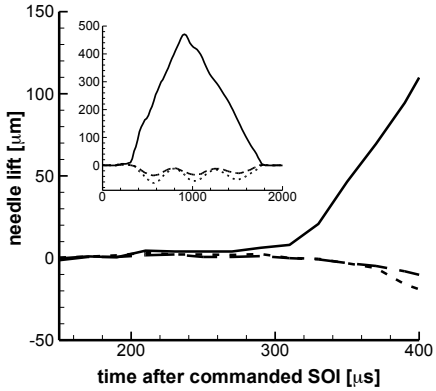

Figure 3. Trajectory of the needle with respect to the cap. The insert shows the complete trajectory of the needle, in the same units.

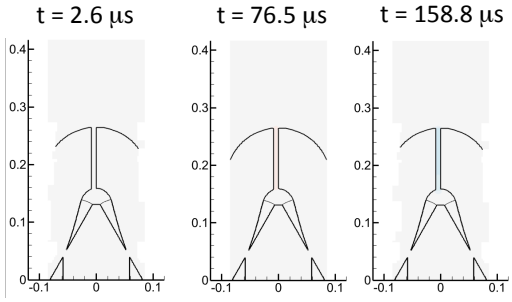

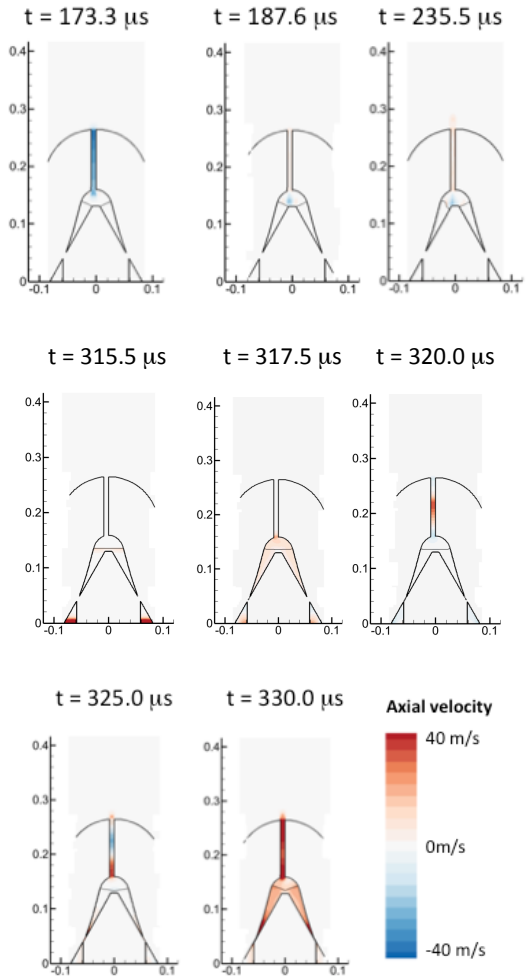

Figure 4. Axial velocity of the gas and liquid phase in the early opening transient as captured by the z = 0 cross-section of the domain. The thicker continuous line corresponds to the intersection with the solid walls of the injector, while the thinner line represents the free surface of the liquid.

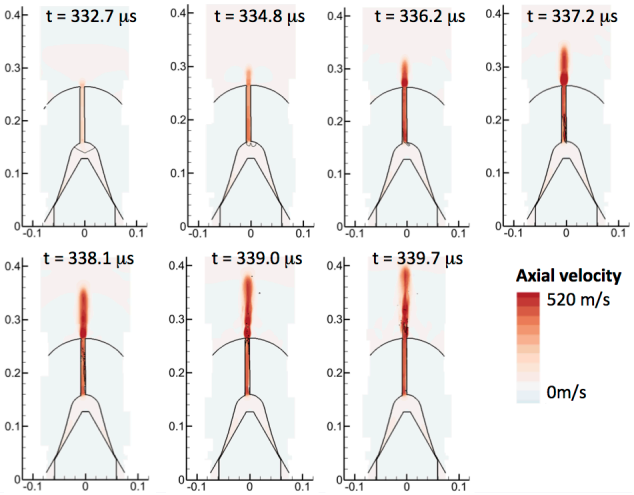

Figure 5. Axial velocity of the gas and liquid phase in the early opening transient as captured by the z = 0 cross-section of the domain. The thicker continuous line corresponds to the intersection with the solid walls of the injector, while the thinner line represents the free surface of the liquid.

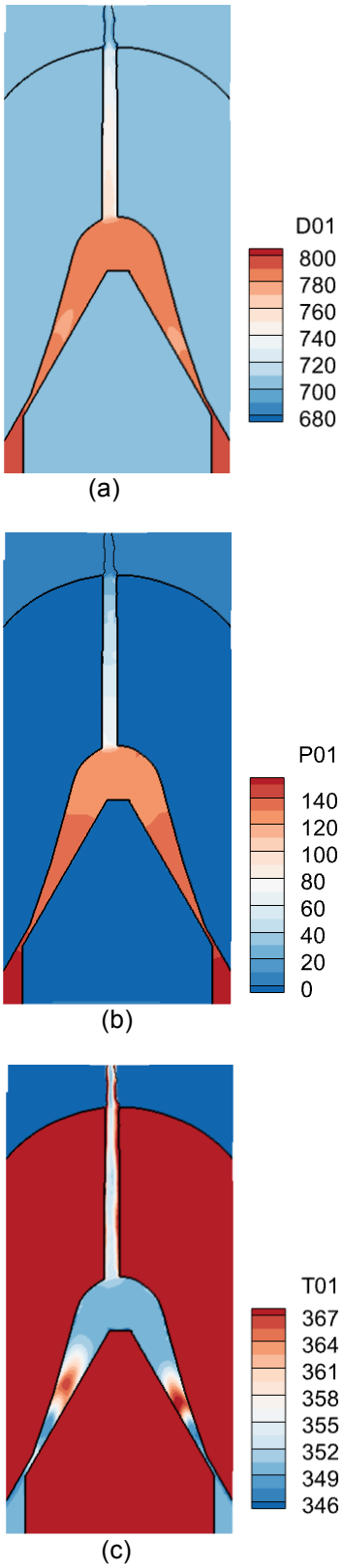

Figure 6. Distribution of (a) density (kg/m^3), (b) pressure (MPa), and (c) temperature (degrees Kelvin) at z = 0 for injector walls at fixed temperature.

RESULTS

INTERNAL FLOW

The simulation begins with a partially liquid-filled sac. The volume left to the gas is 0.065 mm^3, or approximately one third of the sac volume. The volume of the cylindrical orifice, of nominal diameter 90 μm, is much smaller, 0.006 mm^3. A partially filled sac setup is motivated by the observation (via long-distance microscopy and high-contrast display) that a gas or vapor jet is ejected from the orifice before the liquid (Pickett et al., 2013). For the same injection configuration that is studied here, the ejection was reported to take place approximately 7 μs before the exit of the fuel, suggesting that a certain amount of gas or vapor is already in the sac prior to injection.

A sequence related to the first part of the needle lifting is displayed in Figure 4, where time is counted from the activation of the needle. The simulation indicates that gas from outside the injector is actually sucked in, from approximately t = 173 μs to 180 μs. This short-duration flow is due to the receding motion of the needle's tip while the sac is still sealed off from the fuel reservoir: the tip motion is almost imperceptible in this time interval, but the volume displacement is sufficient to cause suction. Thus, at time t = 235.5 μs, the inverted gas jet can be seen to affect the free surface of the fuel.

The obstruction to new liquid entering the cavity begins to be removed a few tens of microseconds later, as the needle begins to lift. This is shown in Figure 4 at t = 315.5 μs by the sudden velocity increase at the bottom of the domain. Note that gaps are still not visible in the z = 0 cross-section because, as noted before, the lifting of the tip is not axis-symmetrical. The injection process is in fact interrupted a few microseconds later because of the wobbling motion of the needle, that causes the free surface to slightly oscillate: it is only by t = 330 μs that the fuel passage completely opens and fuel injection begins.

Once the needle tip is sufficiently removed from the cap's walls, the liquid begins to fill the sac very rapidly. Two main phenomena can be observed at this stage. The first is the asymmetric filling of the orifice that leaves a small pocket of trapped gas at the orifice inlet. This occurrence can be tracked back to the out-of-axis position of the orifice with respect to the injector. Several smaller bubbles can also be observed. The volume occupied by the residual gas is a small percentage of the initial gas volume, approximately 3×10^{-4} mm^3, or 0.15% of the sac volume. The bubble is eventually removed at later stages of the simulation.

The second phenomenon is that when the gas is pushed outside of the orifice, it reaches supersonic conditions that persist until the orifice volume is replaced by fuel. At time t = 337.2 μs, the gas has reached a Mach number of 1.2 at the orifice exit and it is expanding outside the injector above Mach two. Approximately two orifice diameters downstream of the injector's exit, pressure has decreased along the axial direction to 0.057 MPa. The features of the under-expanded jet and the accompanying barrel shock (with axial compression ratio of 4.5) can be partially observed in the second part of the sequence of plots in Figure 5.

EXTERNAL FLOW

The fuel emerges from the orifice at 340 μs. It can be expected that this time delay from SOI depends on the amount of residual gas volume inside the sac, and that it may change between injection cycles. At this point the liquid in the sac has reached a pressure of approximately 100 MPa, that is, a factor of 50 times more than the external value of 2 MPa. In the case of adiabatic walls, the temperature of the fuel in the sac increases following compression by up to five degrees Kelvin, but then decreases again in the expansion at the entrance of the orifice. The fuel temperature is approximately 340 K across the orifice and outside of the injector. A similar trend, but more accentuated, can be seen in the second simulation with isothermal walls (T_w = 383 K) displayed in Figure 6. Temperature increases, and density slightly decreases, soon after the fuel passes the needle's gap and enters the sac, where pressure is still of the order of 120 MPa. The temperature at the orifice exit is on average 358 K in this isothermal walls case, approximately 25 K larger than in the adiabatic case. We note that the density variation displayed in Figure 6 is quite substantial: from 790 kg/m^3 under compression upstream of the needle gap to 700 kg/m^3 at the exit of the injector.

Because of the large injection pressure, the velocity of the fuel at the exit of the orifice is between 450 and 500 m/s. This is a supersonic value compared to the gas phase, but less than half the speed of sound for dodecane. The shape of the tip of the jet that emerges from the injector is far from the regular cylinder, sometimes terminated by a half sphere, which is often assumed as initial condition of injection simulations. Its irregular shape is due to the non-uniform push of the liquid into the sac and is accentuated by the asymmetry of the geometry that was purposely introduced. Observation of later stages of the simulation suggests the interaction with the gas phase is also affected: despite the velocity of the jet is significantly above the speed of sound of air at those conditions, once the fuel exits the injector the compression of the gas is not uniform and does not lead to the formation a sustained shock ahead of the tip of the jet. In fact, the bulk of the jet seems to be preceded by a group of relatively large droplets and ligaments traveling together (see Figure 8), rather than as the mushroom-shaped front tip that appears in other studies (for instance, Shinjo, and Umemura, 2011).

The penetration of the jet emerging from the injector is compared in Figure 9 to the radiographic measures carried out at Argonne, showing that the ROI is reasonably well matched. Penetration in the simulation is measured as the distance from the injector's end of the furthest point of the contiguous jet. This criterion becomes increasingly blurry, however, as the pictures in Figure 8 show.

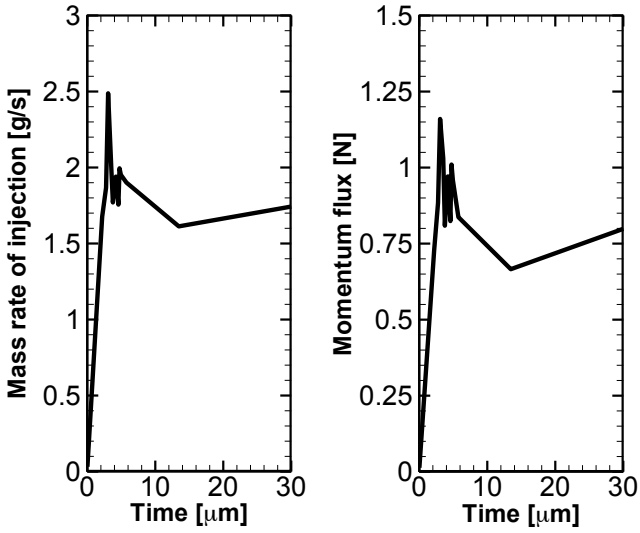

Figure 7. Mass rate and momentum flux from the adiabatic wall simulation.

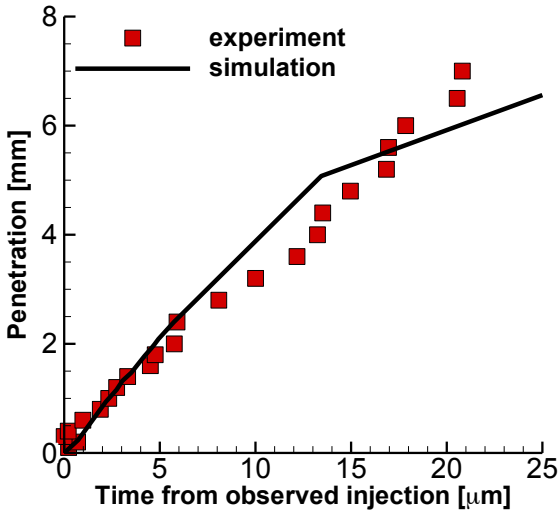

Figure 9. Fuel jet penetration compared with experimental data from the adiabatic wall simulation.

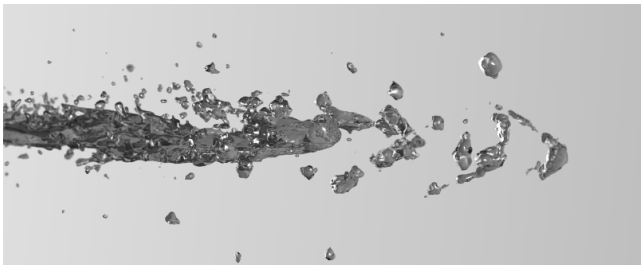

t = 344 μs

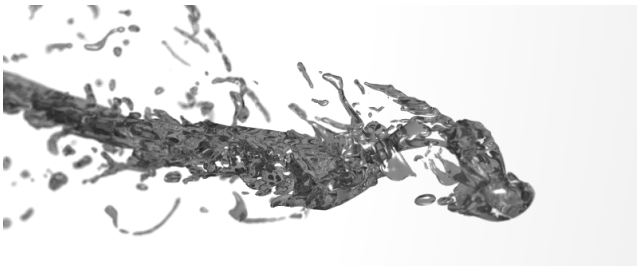

t = 352 μs

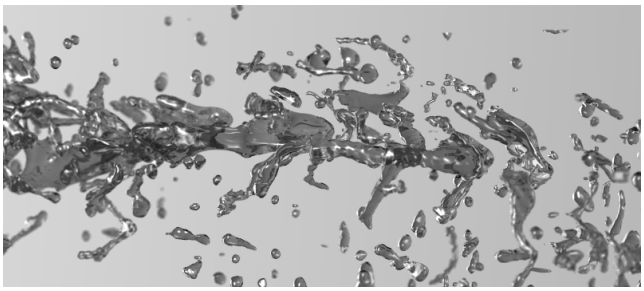

t = 369 μs

Figure 8. Snapshot sequence of ray-tracing rendering of the jet tip (time is from SOI) from the adiabatic wall simulation.

CONCLUSIONS

We have examined the early transient of needle unseating, corresponding to the first 370 μm from activation. Of these, the last 30 μm concern the exit of the fuel from the injector and the formation of a spray. The calculation demonstrates the ease of the proposed methodology for dealing with moving boundaries and for including compressibility effects of the liquid phase.

• At the onset of needle lifting a small amount of gas is sucked into the sac due to a certain amount of interference between needle tip and injector walls.

• This gas and any residual amount in the sac are ejected very rapidly as soon as the needle is activated, exhibiting the characteristics of an under-expanded gas jet immediately outside the orifice.

• At adiabatic wall conditions, the fuel temperature at the orifice exit remains within a few degrees Kelvin from the reservoir temperature of 343 K. The exit temperature is larger in the isothermal calculation by approximately 25 K.

• The calculated rate of injection and momentum are slightly slower that predicted by models based on the injection pressure and an assigned discharge rate. This result requires further investigation.

• Due to the non-uniform filling of the sac, the liquid exits the jet without causing a coherent compression of the gas. For several orifice diameters we observe that the liquid moves faster than the speed of sound in the gas phase without forming a system of shock waves.

In closing, we note that the actual Reynolds numbers that could be resolved in the simulation are quite small.

By construction, the embedded boundary method does not allow for efficient grid spacing near the walls, so that capturing the correct boundary layer thickness remains a challenge. The use of wall functions might reduce this issue. Looking forward, the continuation of the present set of simulations will have to contend with the fact that the processes of injection and spray formation become a formidably "stiff" problem at the scales resolved by the simulation because the stable time-step is six orders of magnitude smaller than the injection cycle period.

ACKNOWLEDGMENTS

Support by Sandia National Laboratories' LDRD (Laboratory Directed Research and Development) is gratefully acknowledged. Sandia National Laboratories is a multi-program laboratory managed and operated by Sandia Corporation, a wholly owned subsidiary of Lockheed Martin Corporation, for the U.S. Department of Energy's National Nuclear Security Administration under contract DE-AC04-94AL85000.

REFERENCES

1. Arienti, M. and Sussman, M., "An Embedded Level Set Method for Sharp-Interface Multiphase Simulations of Diesel Injectors." Int. J. of Multiphase Flow 59: 1-14 (2014).
2. Bode, M., Diewald, F., Broll, D., Heyse, J., le Chenadec, V., and Pitsch, H., "Influence of the Injector Geometry on Primary Breakup in Diesel Injector Systems," SAE Technical Paper 2014-01-1427, 2014.
3. Caudwell, D.R., Trusler, J.P.M., Vesovic, V. and Wakeham, W.A., "The Viscosity and Density of n-Dodecane and n-Octadecane at Pressures up to 200 MPa and Temperatures up to 473 K." International Journal of Thermophysics, Vol. 25, No. 5, 2004.
4. CCSE 2012. https://ccse.lbl.gov/BoxLib/index.html
5. ECN 2013. http://www.sandia.gov/ecn/cvdata/targetCondition/injectorNozGeom.php
6. ECN2 Proceedings, http://www.sandia.gov/ecn/workshop/ECN2.php, Jan. 2014.
7. Jemison, M., Loch, E., Sussman, M., Shashkov, M., Arienti, M., Ohta, M. and Wang, Y. "A Coupled Level Set-Moment of Fluid Method for Incompressible Two-Phase Flows." J. of Scientific Computing, pp. 54:454-491, 2013.
8. Jemison, M., Sussman, M., and Arienti, M., "Compressible, Multi-Phase Semi-Implicit Method with Moment of Fluid Interface Representation." J. of Computational Physics, 279,182-217 (2014).
9. Kadiouglu, S. Y. and Sussman, M., 2008. "Adaptive Solution Techniques for Simulating Underwater Explosions and Implosions." J. of Comp. Phys. 227:2083-2104.
10. Khasanshin, T. S., Shchamialiou, A. P., and Poddubskij, O. G., "Thermodynamic Properties of Heavy n-Alkanes in the Liquid State: n-Dodecane." International Journal of Thermophysics, Vol. 24, No. 5, 2003.
11. Kastengren, A. L., Tilocco, F. Z., Powell, C. F. Manin, J., Pickett, L. M., Payri, R., and Bazyn, T. (2012) "Engine Combustion Network (ECN): Measurements of Nozzle Diameter and Hydraulic Behavior of Diesel Sprays." Atomization and Sprays, 19(11): 1031-1044.
12. Padilla-Victoria, H., Iglesias-Silva, G. A., Ramos-Estrada, M., Hall K. R., 2013. "A correlation to predict speed of sound in liquids: 1. n-Alkanes ($\geq C_5$) and their mixtures at high pressures. " Fluid Phase Equilibria 338 119-127.
13. Pickett, L., Manin, J., Payri, R., Bardi, M., and Gimeno, J., "Transient Rate of Injection Effects on Spray Development." SAE Technical Paper 2013-24-0001, 2013.
14. Pickett, L., Manin, J., Kastengren, A., and Powell, C., "Comparison of Near-Field Structure and Growth of a Diesel Spray Using Light-Based Optical Microscopy and X-Ray Radiography," *SAE Int. J. Engines* 7(2): 1044-1053, 2014.
15. Shinjo, J. and Umemura, A. (2011). "Detailed simulation of primary atomization mechanisms in Diesel jet sprays (isolated identification of liquid jet tip effects)." Proceedings of the Combustion Institute 33 2089-2097
16. Xue, Q., Som, S., Battistoni, M., Longman, D. E. Zhao, H., Senecal, P. K. and Pomraning, E. "Three-dimensional Simulations of the Transient Internal Flow in a Diesel Injector: Effects of Needle Movement". In ILASS Americas, 25th Annual Conference on Liquid Atomization and Spray Systems, Pittsburgh, PA, May 2013.